

## Article

# Pattern Reconstruction of 3-D Modular Antennas by Means of a Non-Redundant Near-Field Spherical Scan

Francesco D'Agostino <sup>1</sup>, Flaminio Ferrara <sup>1</sup>, Claudio Gennarelli <sup>1,\*</sup>, Rocco Guerriero <sup>1</sup> and Giovanni Riccio <sup>2</sup>

<sup>1</sup> Department of Industrial Engineering, University of Salerno, Via Giovanni Paolo II, 84084 Fisciano, Italy; fdagostino@unisa.it (F.D.); flferrara@unisa.it (F.F.); rguerriero@unisa.it (R.G.)

<sup>2</sup> Department of Information and Electrical Engineering and Applied Mathematics, University of Salerno, Via Giovanni Paolo II, 84084 Fisciano, Italy; griccio@unisa.it

\* Correspondence: cgennarelli@unisa.it; Tel.: +39-089-96-4297

**Abstract:** A very flexible source model is proposed here to reduce the volumetric redundancy when considering the pattern reconstruction of three-dimensional modular antennas by means of a near-field spherical scan using a non-redundant sampling representation. Since this last facet is based on the appropriate choice of antenna model for the evaluation of the optimal parameters to be used, the proposed geometry guaranteed the minimum number of needed samples and then a significant time saved for data acquisition on the near-field spherical grid. Then, an optimal interpolation algorithm used these non-redundant samples for an accurate evaluation of the near-field data that were usable in the classical near-field to far-field transformation. The reliability and accuracy of the reconstruction process were proven by means of numerical tests. These last showed a remarkable reduction (about 53%) in needed near-field samples as compared to those required by the classical near-field to far-field transformation and this was achieved without any loss in accuracy.

**Keywords:** volumetric antenna measurements; near-field to far-field transformation techniques; non-redundant sampling representation of electromagnetic fields; spherical scanning



**Citation:** D'Agostino, F.; Ferrara, F.; Gennarelli, C.; Guerriero, R.; Riccio, G. Pattern Reconstruction of 3-D Modular Antennas by Means of a Non-Redundant Near-Field Spherical Scan. *Electronics* **2022**, *11*, 2060. <https://doi.org/10.3390/electronics11132060>

Academic Editor: Reza K. Amineh

Received: 8 June 2022

Accepted: 28 June 2022

Published: 30 June 2022

**Publisher's Note:** MDPI stays neutral with regard to jurisdictional claims in published maps and institutional affiliations.



**Copyright:** © 2022 by the authors. Licensee MDPI, Basel, Switzerland. This article is an open access article distributed under the terms and conditions of the Creative Commons Attribution (CC BY) license (<https://creativecommons.org/licenses/by/4.0/>).

## 1. Introduction

Near-field (NF) and far-field (FF) measurements are usually performed to characterize the radiation performance of an antenna under test (AUT). The measurement region is selected taking into account the specific for which use the AUT is designed. E.g., antennas in radio frequency identification (RFID) systems must satisfy specific NF requirements and, therefore, there is no choice, whereas antennas for terrestrial and satellite links can take advantage of NF or FF acquisition depending on available facilities and resources. Peculiarities, advantages, and disadvantages of NF versus FF measurements are well-known to engineers and researchers working on this topic. Obviously, a proper NF–FF transformation technique is needed if NF data are used for FF pattern reconstruction [1–7]. Planar, cylindrical, and spherical NF–FF transformation techniques are associated to planar, cylindrical, and spherical NF scanning surfaces, respectively, and utilize the corresponding modal expansion of the AUT near field to achieve the FF pattern. In this framework, a special mention must be reserved for the spherical NF–FF transformation as it is the only one that guarantees knowledge of the full radiation pattern. On the other hand, it is the most complicated from analytical and computational viewpoints, so that many efforts have been spent on its optimization (see [8–26] as a non-exhaustive list of references). In particular, for keeping accuracy, the reduction in the time needed to perform the NF measurements is a key point of optimization strategies since it is much longer than that required to realize the NF–FF transformation (usually attained offline). With the same acquisition system, this diminution is certainly achieved by reducing the number of samples to be measured, and a non-redundant sampling representation of the electromagnetic (EM) field radiated by the AUT is useful to this goal. Accordingly, the analytical results in [27,28] have been

exploited in recent years to overcome “the minimum sphere rule” [13] that fixes the number of parallels and the same number of NF samples on each parallel in accordance with the radius of the minimum sphere enclosing the AUT. As a matter of fact, according to these results, the smaller the area of surface enclosing the AUT, the lower the number of required NF samples. In particular, an appropriate choice of the AUT model permits the evaluation of the optimal parameters to be used and the reduction in the number of parallels and samples on them when going toward the poles [14–17]. Unfortunately, the AUT models proposed so far cannot best fit the geometry of some volumetric radiating systems such as those mounted on modular CubeSats. These nanosatellites follow the popular “CubeSat project” standard [29] and are made up of multiple cubic units with sides of 10 cm, e.g., a 3-U CubeSat is composed of three units stacked lengthwise. The minimum sphere can be adopted as source model for a 1-U CubeSat, but prolate spheroids or cylinders terminated by two spherical caps do not minimize the volumetric redundancy of the source model for an  $n$ -U CubeSat. Please remember that a closed cylindrical surface cannot be conveniently used in the context of the non-redundant sampling representations, since the unit vector normal to the surface possesses discontinuities when crossing the circular contours of the bases.

A very flexible source model (see Figure 1) is proposed here to minimize the volumetric redundancy when considering the pattern reconstruction of 3-D modular AUTs by means of a spherical NF scan using a non-redundant sampling representation.

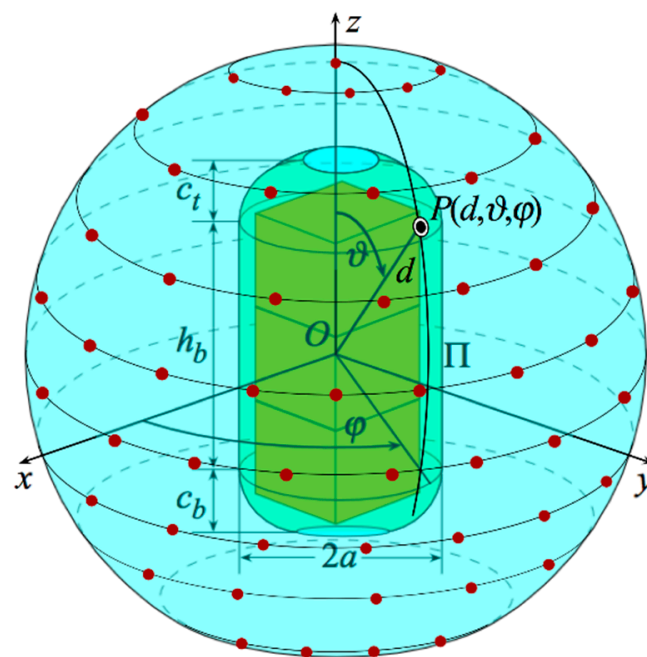


**Figure 1.** Spherical scan using a very flexible model for 3-D modular AUTs.

A central cylindrical body ended by two circular bowls with same apertures and different bases forms the proposed envelope. Note that, on the contrary of prolate spheroids and cylinders terminated by spherical caps having only two geometrical degrees of freedom, the composite surface in Figure 1 possesses four geometrical degrees of freedom, i.e., height and radius of the central body and radii of the lateral bendings, thus permitting the best fit for the geometry of 3-D modular radiating systems regardless their modules are arranged. Accordingly, it minimizes the volumetric redundancy, contains the spherical and flexible models [15,17] as particular cases, and, for keeping accuracy, guarantees a non-redundant number of needed samples, thus saving a significant time for the data acquisition. An optimal sampling interpolation (OSI) algorithm is subsequently developed to use these non-redundant data for an accurate computation of the NF values that are utilizable in the classical NF–FF transformation [13].

Accounting for the above statements, it is evident that the source model proposed here represents a good innovation in the spherical NF–FF transformation exploiting the non-redundant sampling representations, since it is much more flexible and contains the other models as particular cases.

The paper is organized as follows. In Section 1, the interests and motivations justifying the development of a non-redundant NF–FF transformation particularly suitable for dealing with 3-D modular antennas are stressed. In Section 2, an effective sampling representation of the voltage acquired by the measuring probe over the scanning sphere is developed by properly applying the non-redundant representations of EM fields [27,28] and assuming 3-D modular radiating systems as contained in the proposed envelope. A two-dimensional OSI formula allowing one to accurately reconstruct the probe voltage at any point on the scanning sphere from a non-redundant number of its samples is also developed in the same section. Numerical results, assessing the effectiveness of the so-developed OSI representation and of the corresponding NF–FF transformation, are shown in Section 3. At last, conclusions are drawn in Section 4.

## 2. Sampling Representation over a Sphere from a Minimum Number of NF Samples

This section is devoted to the development of a non-redundant sampling representation of the voltage acquired by a non-directive first-order probe over the measurement sphere from a minimum number of its samples, which is particularly effective in the case of volumetric, 3-D modular, AUTs. To this end, let us suppose to perform the characterization of such a kind of AUT in a spherical NF facility and to set the radius  $R_S$  of the scanning sphere in such a way that it is in the antenna NF region. Moreover, let us adopt the spherical coordinate system  $(r, \nabla, \Pi)$  to specify an observation point  $Q$ .

According to [27], the development of an effective non-redundant representation of the voltage acquired by the adopted probe over the sphere proceeds as follows: (1) the AUT is assumed as contained in a convex domain delimited by a rotational surface  $S$ , (2) a proper analytical parameterization  $\underline{r} = \underline{r}(\eta)$  is adopted to represent each of the curves  $\Pi$  (meridians and parallels) describing the measurement sphere, and (3) a suitable phase factor  $e^{-j\psi(\eta)}$  is extracted from the voltage expression  $V$  of the probe ( $V_p$ ) and rotated probe ( $V_r$ ). These steps make possible to introduce the so-called “reduced voltage”

$$\tilde{V}(\eta) = V(\eta)e^{j\psi(\eta)} \quad (1)$$

which is a spatially quasi-bandlimited function [27], whose bandwidth  $W_\eta$  practically coincides, for the considered probe, with that of the EM field radiated by the AUT [30]. The error arising when such a function is approximated by a strictly bandlimited one can be minimized by choosing an approximating function with an enlarged bandwidth  $\chi'W_\eta$ , with  $\chi'$  being an enlargement bandwidth factor. A value of  $\chi'$  slightly larger than unity is enough for electrically large AUTs [27].

When  $\Pi$  is a meridian, the expressions of the bandwidth  $W_\eta$ , the optimal parameter  $\eta$  and phase function  $\psi$  are [15,17,27]:

$$W_\eta = \ell' / \lambda \quad (2)$$

$$\eta = (\pi / \ell') [D_1 - D_2 + \tau'_1 + \tau'_2] \quad (3)$$

$$\psi = (\pi / \lambda) [D_1 + D_2 + \tau'_1 - \tau'_2] \quad (4)$$

where  $\lambda$  is the free-space wavelength and  $\ell'$  is the length of the curve  $\Pi'$ , obtained as intersection of the surface  $S$  with the meridian plane through the observation point  $Q$ ,  $D_{1,2}$  are the distances of  $Q$  from the two tangency points  $Q_{1,2}$  on  $\Pi'$ , and  $\tau'_{1,2}$  are their curvilinear coordinates.

When  $\Pi$  is a parallel identified by the angle  $\vartheta$ ,  $\psi$  becomes constant, the angular parameter  $\varphi$  can be conveniently used for representing it, and the related bandwidth [15,17] is

$$W_\varphi = \frac{\pi}{\lambda} \max_{z'}(D^+ - D^-) = \frac{\pi}{\lambda} \max_{z'} \left( \sqrt{(z - z')^2 + (\rho + \rho'(z'))^2} - \sqrt{(z - z')^2 + (\rho - \rho'(z'))^2} \right) \tag{5}$$

where  $D^+, D^-$  are the maximum and minimum distances from  $\Pi$  to the circumference of  $S$  at  $z'$ , respectively,  $\rho = R_S \sin \vartheta$ , and  $\rho'(z')$  represents the equation of  $S$  in cylindrical coordinates. As shown in [15,17,27], the maximum is on the zone of the surface  $S$ , which lies on the same side of the observation circumference with respect to its maximum transverse circle.

It must be stressed that the choice of the modeling surface enclosing the AUT plays a key role in the development of an effectively non-redundant representation. It must be a regular surface, which must fit the AUT geometry as much as possible. In fact, as shown in [27], the overall number  $N$  of samples at Nyquist spacing on any closed observation surface (also unbounded) surrounding the AUT is given by:

$$N \cong \frac{\text{area of } S}{(\lambda/2)^2} \tag{6}$$

Thus, the smaller the area of  $S$ , the lower the number of required NF samples. Unfortunately, when dealing with volumetric 3-D modular AUTs, such as those mounted on modular CubeSats, the spherical AUT model, as well as those proposed in [14–17], do not minimize the area of the modeling surface  $S$ . To this end, a very flexible source model (Figure 1) is here proposed. It is formed by a central cylindrical body of height  $h_b$  and radius  $a$ , ended by two circular bowls with same aperture diameter ( $2a$ ) and different lateral bendings with radii  $c_t$  and  $c_b$ . Note that, unlike the AUT models proposed in [14–17], which have only two or three geometrical degrees of freedom, the proposed surface has four geometrical degrees of freedom, thus allowing a best fitting of the geometry of 3-D modular AUTs. It must be stressed that such an AUT model contains the spherical and flexible models [15] as particular cases. As a matter of fact, when  $h_b$  is set to zero and  $c_t$  and  $c_b$  are both set to  $a$ ,  $S$  becomes a spherical surface, when  $h_b$  is set to zero,  $S$  reduces to a double bowl, and, when  $c_t$  and  $c_b$  are both set to  $a$ ,  $S$  becomes a rounded cylinder.

When adopting such a model, the length of the curve  $\Pi'$  is  $\ell' = 2[h_b + b_t + b_b + \pi/2(c_t + c_b)]$ , wherein  $b_t = a - c_t$  and  $b_b = a - c_b$ , and the parameters  $D_{1,2}$  and  $\tau'_{1,2}$ , which are involved in relations (3) and (4) to evaluate  $\eta$  and  $\psi$ , can be determined by properly taking into account the position of the tangency points  $Q_{1,2}$  on  $\Pi'$ . Five cases occur for  $\vartheta$  ranging in  $[0, \pi]$  (see Figure 2a). Accordingly, when  $\vartheta$  belongs to the range  $[0, \vartheta_A]$ , where  $\vartheta_A = \sin^{-1}(a/R_S)$ , it follows:

$$D_1 = \sqrt{R_S^2 + f^2 - 2R_S f \cos(\delta + \vartheta) - c_t^2} \cdot \tau'_1 = -(b_t + c_t \gamma_1) \tag{7}$$

$$\gamma_1 = \tan^{-1}(D_1/c_t) - \tan^{-1}[(b_t + R_S \sin \vartheta)/(R_S \cos \vartheta - h_b/2)] \tag{8}$$

$$D_2 = \sqrt{R_S^2 + f^2 - 2R_S f \cos(\delta - \vartheta) - c_t^2} \cdot \tau'_2 = b_t + c_t \gamma_2 \tag{9}$$

$$\gamma_2 = \tan^{-1}(D_2/c_t) - \tan^{-1}[(b_t - R_S \sin \vartheta)/(R_S \cos \vartheta - h_b/2)] \tag{10}$$

being  $f = \sqrt{b_t^2 + (h_b/2)^2}$  and  $\delta = \tan^{-1}(2b_t/h_b)$ . When  $\vartheta$  belongs to the range  $[\vartheta_A, \vartheta_B]$ , where  $\vartheta_B = \cos^{-1}[(h_b/2 + c_t)/R_S]$ ,  $D_1$  and  $\tau'_1$  are again given by (7), whereas

$$D_2 = \sqrt{R_S^2 + f'^2 + 2R_S f' \cos(\delta' + \vartheta) - c_b^2} \cdot \tau'_2 = b_t + c_t \pi/2 + h_b + c_b \gamma_2 \tag{11}$$

$$\gamma_2 = \tan^{-1}(D_2/c_b) - \tan^{-1}[(h_b/2 + R_S \cos \vartheta)/(R_S \sin \vartheta - b_b)] \tag{12}$$

being  $f' = \sqrt{b_b^2 + (h_b/2)^2}$  and  $\delta' = \tan^{-1}(2b_b/h_b)$ . When  $\vartheta$  belongs to the range  $[\vartheta_B, \vartheta_C]$ , where  $\vartheta_C = \pi - \cos^{-1}[(h_b/2 + c_b)/R_S]$ ,  $D_2$  and  $\tau'_2$  are again expressed by (11), whereas

$$D_1 = \sqrt{R_S^2 + f^2 - 2R_S f \cos(\delta - \vartheta) - c_t^2} \cdot \tau'_1 = b_t + c_t(\pi/2 + \gamma_1) \tag{13}$$

$$\gamma_1 = -\left\{ \tan^{-1}(D_1/c_t) + \tan^{-1}[(R_S \cos \vartheta - h_b/2)/(R_S \sin \vartheta - b_t)] \right\} \tag{14}$$

When  $\vartheta$  belongs to the range  $[\vartheta_C, \vartheta_D]$ , where  $\vartheta_D = \pi - \sin^{-1}[a/R_S]$ ,  $D_1$  and  $\tau'_1$  are again given by (13), whereas

$$D_2 = \sqrt{R_S^2 + f'^2 + 2R_S f' \cos(\delta' - \vartheta) - c_b^2} \tag{15}$$

$$\tau'_2 = b_t + 2b_b + h_b + (c_t + c_b)\pi/2 + c_b\gamma_2$$

$$\gamma_2 = \tan^{-1}(D_2/c_b) - \tan^{-1}[(R_S \sin \vartheta + b_b)/(|R_S \cos \vartheta| - h_b/2)] \tag{16}$$

Lastly, when  $\vartheta$  belongs to the range  $[\vartheta_D, \pi]$ ,  $D_2$  and  $\tau'_2$  are again expressed by (15), whereas

$$D_1 = \sqrt{R_S^2 + f'^2 + 2R_S f' \cos(\delta' + \vartheta) - c_b^2} \tag{17}$$

$$\tau'_1 = b_t + c_t\pi/2 + h_b + c_b(\pi/2 + \gamma_1)$$

$$\gamma_1 = -\left\{ \tan^{-1}(D_1/c_b) - \tan^{-1}[(b_b - R_S \sin \vartheta)/(|R_S \cos \vartheta| - h_b/2)] \right\} \tag{18}$$

Let us turn now to the evaluation of the maximum in relation (5), which allows one to obtain the azimuthal bandwidth  $W_\varphi$ . It can easily be shown that the maximum is attained at  $z' = z$  if  $|z| < h_b/2$ ; otherwise, it is convenient to introduce the angular coordinate  $\alpha$ , such that (see Figure 2b for the case  $z > h_b/2$ )

$$\begin{cases} z' = h_b/2 + c_t \cos \alpha; & \rho' = b_t + c_t \sin \alpha & \text{if } z > h_b/2 \\ z' = -(h_b/2 + c_b \cos \alpha); & \rho' = b_b + c_b \sin \alpha & \text{if } z < -h_b/2 \end{cases} \tag{19}$$

and then determine the maximum as that value of  $\alpha$  zeroing the derivative of  $D^+ - D^-$  with respect to  $\alpha$ .

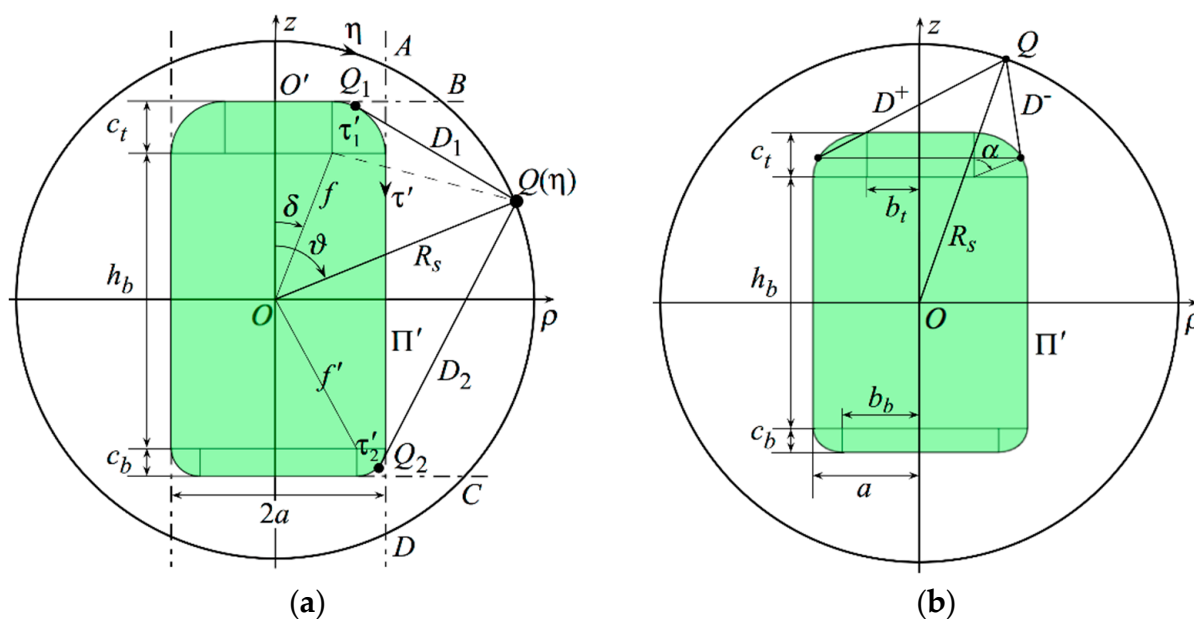


Figure 2. (a) Relevant to the representation along the meridians; (b) relevant to the representation along the parallels.

According to these results, the reconstruction of the voltage  $V$  ( $V_p$  or  $V_r$ ) at a given point  $Q(\vartheta, \varphi)$  on the scanning sphere can be performed by means of the following two-dimensional OSI algorithm, involving an interpolation along the parallels and another one along the meridians. These interpolations are properly accomplished by using efficient one-dimensional OSI expansions [14–17,27], which make use of only a few NF samples around the output point  $Q$ ,  $2q$  along the parallels and  $2p$  along the meridians. Accordingly, once the NF samples  $V(\eta_k, \varphi_{i,k}) = \tilde{V}(\eta_k, \varphi_{i,k})e^{-j\psi(\eta_k)}$  have been collected at the points specified by

$$\eta_k = k\Delta\eta = \frac{2\pi k}{2K'' + 1} \quad \varphi_{i,k} = i\Delta\varphi_k = \frac{2\pi i}{2I_k'' + 1} \tag{20}$$

where

$$K'' = \lfloor \chi K' \rfloor + 1 \quad K' = \lfloor \chi' W_\eta \rfloor + 1 \tag{21}$$

$$I_k'' = \lfloor \chi I_k' \rfloor + 1 \quad I_k' = \lfloor \chi^* W_\varphi(\eta_k) \rfloor + 1 \tag{22}$$

$$\chi^* = 1 + (\chi' - 1) [\sin \vartheta(\eta_k)]^{-2/3}, \tag{23}$$

$\lfloor \cdot \rfloor$  being the floor function and  $\chi$  being an oversampling factor needed to control the truncation error, the voltage reconstruction proceeds as follows. First, the  $2p$  intermediate reduced samples  $\tilde{V}(\eta_k, \varphi)$  at the intersection points between the sampling parallels and the cut plane at  $\varphi$  are reconstructed by means of

$$\tilde{V}(\eta_k, \varphi) = \sum_{i=i_0-q+1}^{i_0+q} \tilde{V}(\eta_k, \varphi_{i,k}) Tch_{I_k}(\varphi - \varphi_{i,k}, \bar{\varphi}_k) Dirch_{I_k''}(\varphi - \varphi_{i,k}) \tag{24}$$

where  $i_0 = \lfloor \varphi / \Delta\varphi_k \rfloor$  is the index of the sample closest to each intersection point,  $\bar{\varphi}_k = q\Delta\varphi_k$ ,  $I_k = I_k'' - I_k'$  and

$$Dirch_{I''}(\varphi) = \frac{\sin[(2I'' + 1)\varphi/2]}{(2I'' + 1) \sin(\varphi/2)} \tag{25}$$

$$Tch_I(\varphi, \bar{\varphi}) = \frac{T_I[2 \cos^2(\varphi/2) / \cos^2(\bar{\varphi}/2) - 1]}{T_I[2 / \cos^2(\bar{\varphi}/2) - 1]} \tag{26}$$

are the Dirichlet and Tschebyscheff Sampling functions, respectively,  $T_I(\cdot)$  being the Tschebyscheff polynomial of degree  $I$ . The value of the voltage  $V$  at  $Q$  is then obtained by interpolating these intermediate reduced samples through

$$V(\eta(\vartheta), \varphi) = e^{-j\psi(\eta)} \sum_{k=k_0-p+1}^{k_0+p} \tilde{V}(\eta_k, \varphi) Tch_K(\eta - \eta_k, \bar{\eta}) Dirch_{K''}(\eta - \eta_k) \tag{27}$$

$k_0 = \lfloor \eta / \Delta\eta \rfloor$  is the index of the sample closest to  $Q$ ,  $\bar{\eta} = p\Delta\eta$ ,  $K = K'' - K'$ , and all other symbols have the same or analogous meanings as in (24).

The two-dimensional OSI formula resulting by combining (24) and (27) is employed to precisely reconstruct the voltages  $V_p$  and  $V_r$  at any point on the measurement sphere and, in particular, at those required to carry out the classical NF–FF transformation with spherical scanning [13].

### 3. Numerical Results

This section is devoted to present some representative numerical results assessing the effectiveness of the proposed non-redundant NF–FF transformation with spherical scanning for 3-D modular AUTs. The considered AUT has been properly arranged to simulate a modular CubeSat, made up of three cubic units with side of  $8\lambda$  realizing a parallelepiped  $8\lambda \times 8\lambda \times 24\lambda$ -sized, which is centered with respect to the adopted  $(x, y, z)$  reference system. An array of elementary Huygens sources, spaced by  $\lambda/2$  and polarized along the  $z$ -axis, is placed on each lateral face, but only that on the face at  $y = 4\lambda$  is considered as fed in the simulations. Moreover, a circular array of radius  $4\lambda$  is placed over each basis

at a distance of  $2\lambda$ . The array elements are, in such a case, elementary Huygens sources with linear polarization along the  $y$ -axis and spaced by  $\lambda/2$  with respect to the  $x$ - and  $y$ -axes. Such an AUT has been assumed as enclosed in the very flexible model surface proposed here, whose parameters have been properly chosen to allow the best possible fitting. Accordingly,  $h_b = 24\lambda$ ,  $a = 6\lambda$ , and  $c_t = c_b = 2\lambda$ . The voltage samples have been simulated as acquired by the measuring probe over a sphere of radius  $R_S = 20\lambda$  at the points prescribed by the non-redundant sampling representation proposed here, adopting the enlargement bandwidth and oversampling factors,  $\chi'$  and  $\chi$ , both equal to 1.20. The used probe is an open-ended rectangular waveguide, which, showing a practically first-order azimuthal dependence [31], can be properly treated as a first-order probe.

To test the precision of OSI Formulas (24) and (27) from a qualitative standpoint, the reconstructions of the amplitudes and phases of the probe and rotated probe voltages,  $V_p$  and  $V_r$ , on the meridians at  $\varphi = 0^\circ$  and  $\varphi = 90^\circ$  are compared in Figures 3 and 4 with the corresponding exact ones. As can be seen, the reconstructed pattern agrees very well with the exact one. To further confirm the precision of these formulas from a more quantitative standpoint, the mean-square reconstruction errors have been evaluated by comparing the exact values of  $V_p$  and  $V_r$  at the points of a dense lattice on the scanning sphere with the recovered ones and normalizing them to the maximum voltage value over the sphere. These errors, evaluated for  $\chi' = 1.20$  and some  $\chi$  and  $p = q$  values, are reported in Figure 5 and show a decreasing behavior as  $\chi$ ,  $p$ , and  $q$  increase. This allows a proper choice of the OSI parameters for a given value of tolerable reconstruction error. Note that the OSI parameters adopted here have been properly chosen in order to guarantee a mean-square reconstruction error of at least  $-70$  dB, which can be considered negligible with respect to the measurement error (about  $-40$  dB). The algorithm robustness with respect to errors affecting the NF data has been also verified. To this end, the exact NF samples have been corrupted with severe random errors, which simulate a background, bounded to  $\Delta\sigma$ (dB) in amplitude and with arbitrary phase, and an uncertainty on each sample of  $\pm\Delta\sigma_r$  (dB) in amplitude and  $\pm\Delta\phi$  (degrees) in phase. As shown in Figure 6, the algorithm results are also stable, since it does not amplify the errors injected on the exact samples.

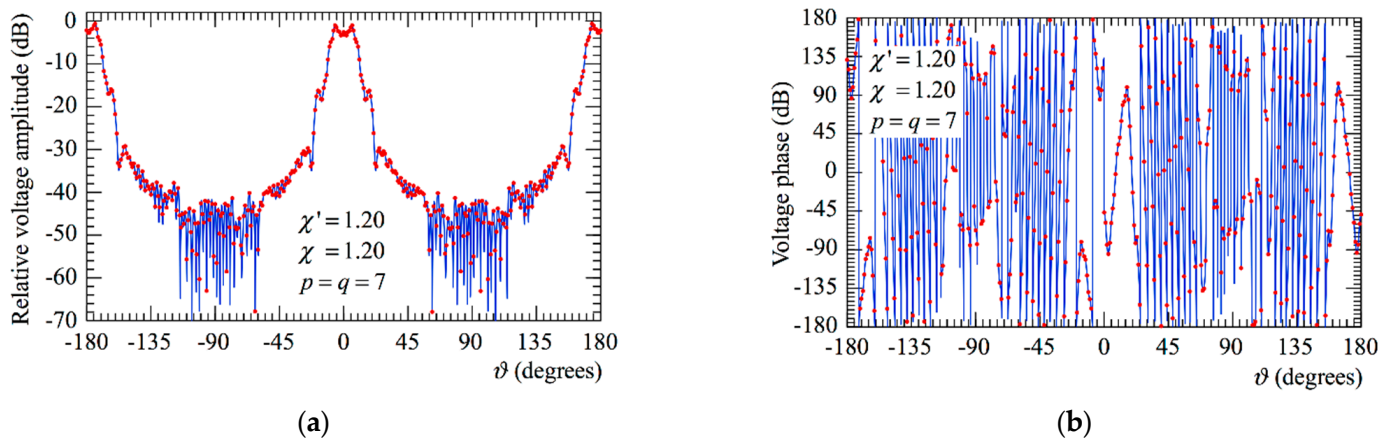


**Figure 3.**  $V_p$  on the meridian at  $\varphi = 0^\circ$ . Blue solid line: exact. Red dots: interpolated from the non-redundant samples: (a) Amplitude; (b) Phase.

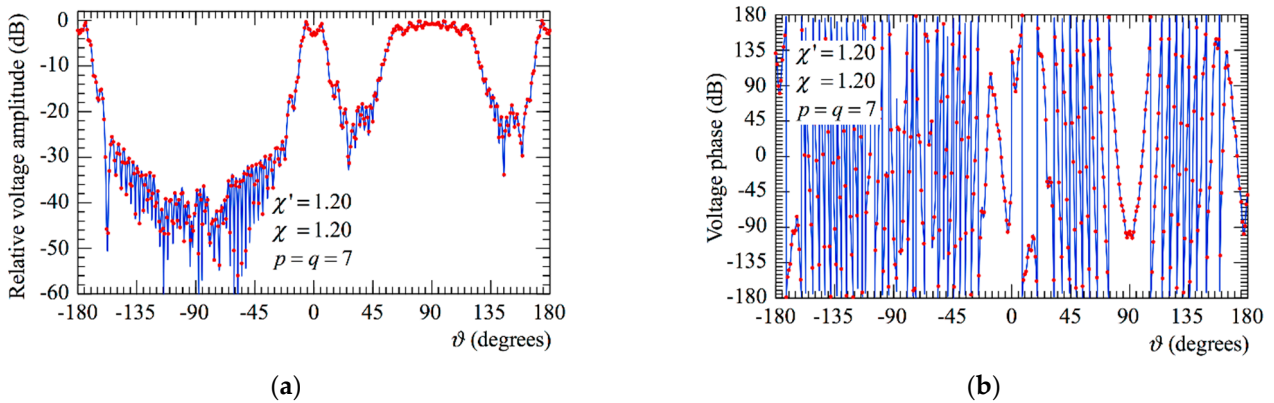


Figure 4.  $V_r$  on the meridian at  $\varphi = 90^\circ$ . Blue solid line: exact. Red dots: interpolated from the non-redundant samples: (a) Amplitude; (b) Phase.

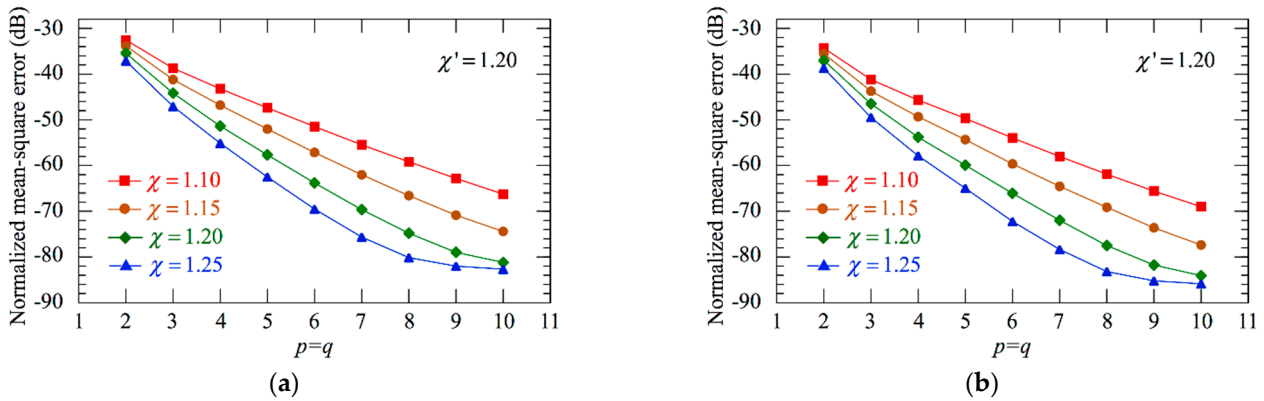


Figure 5. Mean-square errors in the reconstruction of the probe voltage: (a)  $V_r$ ; (b)  $V_p$ .

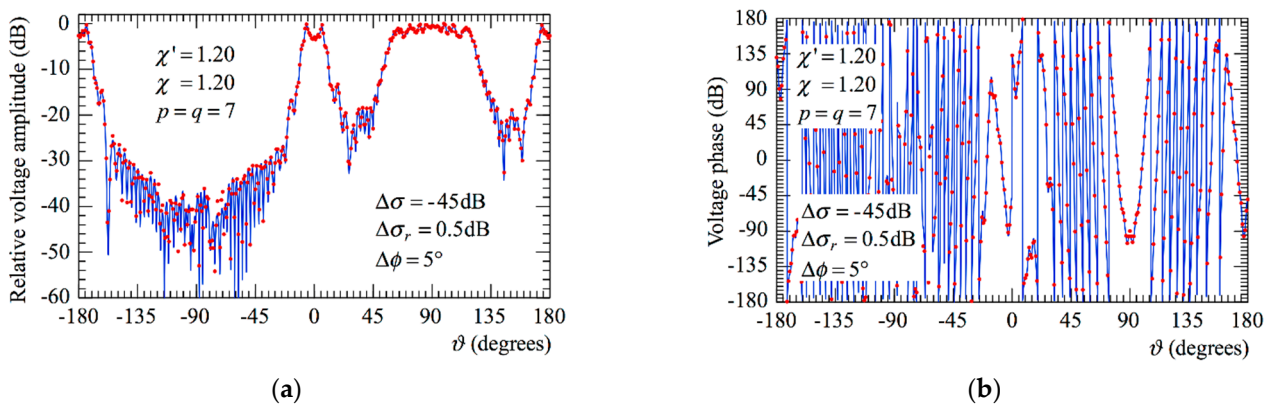
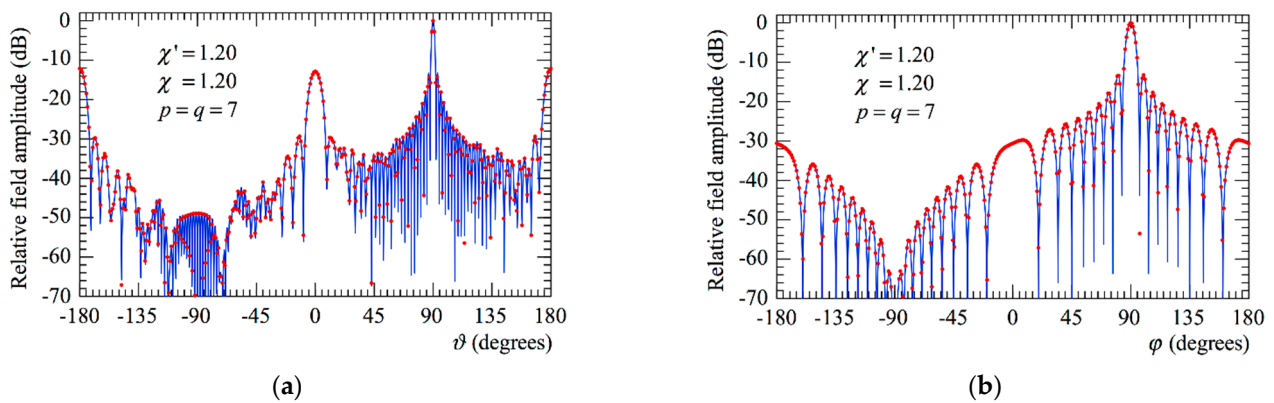
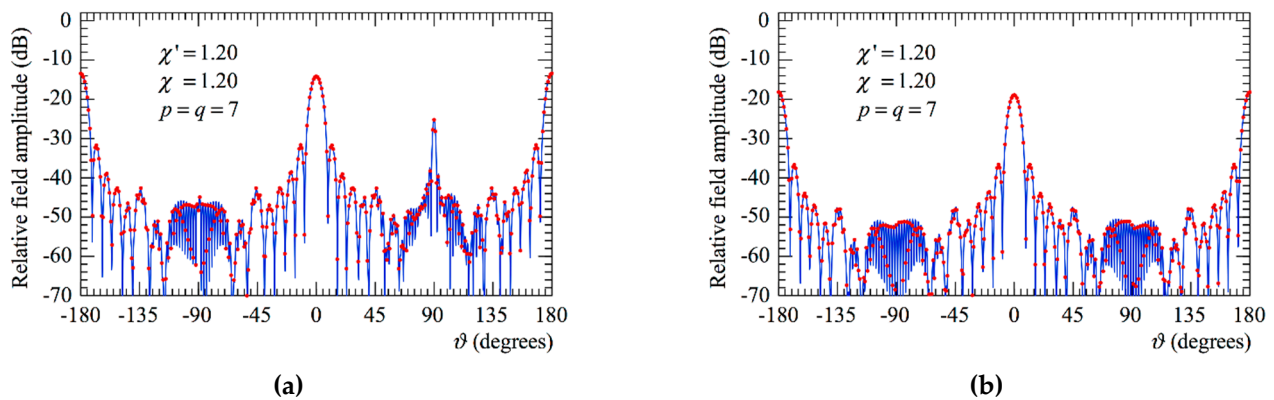


Figure 6.  $V_r$  on the meridian at  $\varphi = 90^\circ$ . Blue solid line: exact. Red dots: interpolated from the non-redundant error affected samples: (a) Amplitude; (b) Phase.

At last, OSI Formulas (24) and (27) have been employed for reconstructing the NF data required to perform the classical probe-compensated NF-FF transformation with spherical scanning [13]. Figure 7 reports the comparison between the so-recovered FF patterns in the principal planes and the corresponding exact ones. A further FF reconstruction example relevant to the cut plane at  $\phi = 60^\circ$  is reported in Figure 8. As can be seen, the exact FF patterns and those recovered from the non-redundant NF samples are in excellent agreement, thus assessing the effectiveness of the proposed spherical NF-FF transformation for 3-D modular AUTs.



**Figure 7.** Far-field pattern. Blue solid line: exact. Red dots: interpolated from the non-redundant samples: (a) E-Plane; (b) H-plane.



**Figure 8.** Far-field pattern in the cut plane at  $\varphi = 60^\circ$ . Blue solid line: exact. Red dots: interpolated from the non-redundant samples: (a) FF  $\theta$ -component; (b) FF  $\varphi$ -component.

It must be stressed that the number of non-redundant NF samples used in such a reconstruction example is 11,034, which compares favorably with that (23,544) which would have been required by the classical spherical NF–FF transformation technique [13].

#### 4. Conclusions

In this paper, a non-redundant NF–FF transformation with spherical scanning, which makes use of a very flexible source model to reduce the volumetric redundancy of 3-D modular AUTs, has been developed. This model results are particularly appealing when dealing with such a kind of AUTs, since a proper choice of its parameters makes it possible to develop a sampling representation which employs the minimum number of NF samples. These samples can be effectively interpolated via an ad hoc developed OSI algorithm to evaluate the NF value at any point of the measurement sphere, and, in particular, at those required by the classical NF–FF transformation with spherical scanning. Since these last depend on the minimum sphere rule, a significant measurement time can be saved. The numerical tests have assessed the reliability of the non-redundant sampling representation and the related OSI reconstruction process. The proposed method for the full pattern reconstruction of the considered AUT uses only the 47% of the NF samples as compared to the classical spherical NF–FF transformation [13]. This percentage obviously depends on the geometric characteristics of the AUT and can increase or decrease when accounting for its volumetric occupancy.

**Author Contributions:** Formal analysis, F.F., C.G., R.G. and G.R.; Investigation, F.F., R.G. and G.R.; Methodology, F.F., C.G., R.G. and G.R.; Software, F.F.; Supervision, C.G.; Validation, F.D. and F.F.; Visualization, C.G.; Writing—original draft, R.G.; Writing—review and editing, F.D., C.G., R.G. and G.R. All authors have read and agreed to the published version of the manuscript.

**Funding:** This research received no external funding.

**Conflicts of Interest:** The authors declare no conflict of interest.

## References

1. Yaghjian, A.D. An overview of near-field antenna measurements. *IEEE Trans. Antennas Propag.* **1986**, *34*, 30–45. [[CrossRef](#)]
2. Appel-Hansen, J.; Dyson, J.D.; Gillespie, E.S.; Hickman, T.G. Antenna measurements. In *The Handbook of Antenna Design*; Rudge, A.W., Milne, K., Olver, A.D., Knight, P., Eds.; Peter Peregrinus: London, UK, 1986; pp. 584–694.
3. Francis, M.H.; Wittmann, R.W. Near-field scanning measurements: Theory and practice. In *Modern Antenna Handbook*; Balanis, C.A., Ed.; John Wiley & Sons Inc.: Hoboken, NJ, USA, 2008; pp. 929–976.
4. Gennarelli, C.; Capozzoli, A.; Foged, L.; Fordham, J.; van Rensburg, D.J. Recent advances in near-field to far-field transformation techniques. *Int. J. Antennas Propag.* **2012**, *2012*, 243203. [[CrossRef](#)]
5. Francis, M.H. *IEEE Recommended Practice for Near-Field Antenna Measurements*; IEEE Standard: Piscataway, NJ, USA, 2012; pp. 1720–2012.
6. Ferrara, F.; Gennarelli, C.; Guerriero, R. Near-field antenna measurement techniques. In *Handbook of Antenna Technologies*; Chen, Z.N., Liu, D., Nakano, H., Qing, X., Zwick, T., Eds.; Springer: Singapore, 2016; pp. 2107–2163.
7. Parini, C.; Gregson, S.; McCormick, J.; van Rensburg, D.J.; Eibert, T. *Theory and Practice of Modern Antenna Range Measurements*; SciTech Publishing IET: London, UK, 2020.
8. Jensen, F. On the probe compensation for near-field measurements on a sphere. *Archiv Elektr. Übertr.* **1975**, *29*, 306–308.
9. Wacker, P.F. *Non-Planar Near-Field Measurements: Spherical Scanning*; NBSIR 75-809; National Bureau of Standards: Boulder, CO, USA, 1975.
10. Larsen, F.H. Probe correction of spherical near-field measurements. *Electr. Lett.* **1977**, *13*, 393–395. [[CrossRef](#)]
11. Yaghjian, A.D.; Wittmann, R.C. The receiving antenna as a linear differential operator: Application to spherical near-field measurements. *IEEE Trans. Antennas Propag.* **1985**, *33*, 1175–1185. [[CrossRef](#)]
12. Hansen, J.E.; Jensen, F. Spherical near-field scanning at the technical university of Denmark. *IEEE Trans. Antennas Propag.* **1988**, *36*, 734–739. [[CrossRef](#)]
13. Hald, J.; Hansen, J.E.; Jensen, F.; Larsen, F.H. *Spherical Near-Field Antenna Measurements*; Hansen, J.E., Ed.; Peregrinus: London, UK, 1998.
14. Bucci, O.M.; Gennarelli, C.; Riccio, G.; Savarese, C. Data reduction in the NF-FF transformation technique with spherical scanning. *J. Electromagn. Waves Appl.* **2001**, *15*, 755–775. [[CrossRef](#)]
15. D’Agostino, F.; Ferrara, F.; Gennarelli, C.; Guerriero, R.; Migliozi, M. Effective antenna modellings for NF-FF transformations with spherical scanning using the minimum number of data. *Int. J. Antennas Propag.* **2011**, *2011*, 936781. [[CrossRef](#)]
16. D’Agostino, F.; Ferrara, F.; Gennarelli, C.; Guerriero, R.; Migliozi, M. Non-redundant spherical NF-FF transformations using ellipsoidal antenna modeling: Experimental assessments. *IEEE Antennas Propag. Magaz.* **2013**, *55*, 166–175. [[CrossRef](#)]
17. D’Agostino, F.; Ferrara, F.; Gennarelli, C.; Guerriero, R.; Migliozi, M. Experimental testing of nonredundant near-field to far-field transformations with spherical scanning using flexible modellings for nonvolumetric antennas. *Int. J. Antennas Propag.* **2013**, *2013*, 517934. [[CrossRef](#)]
18. Laitinen, T.; Pivnenko, S.; Nielsen, J.M.; Breinbjerg, O. Theory and practice of the FFT/matrix inversion technique for probe-corrected spherical near-field antenna measurements with high-order probes. *IEEE Trans. Antennas Propag.* **2010**, *58*, 2623–2631. [[CrossRef](#)]
19. Hansen, T.B. Spherical near-field scanning with higher-order probes. *IEEE Trans. Antennas Propag.* **2011**, *59*, 4049–4059. [[CrossRef](#)]
20. Hansen, T.B. Numerical investigation of the system-matrix method for higher-order probe correction in spherical near-field antenna measurements. *Int. J. Antennas Propag.* **2012**, *2012*, 493705. [[CrossRef](#)]
21. Qureshi, M.A.; Schmidt, C.H.; Eibert, T.F. Adaptive sampling in spherical and cylindrical near-field antenna measurements. *IEEE Antennas Propag. Magaz.* **2013**, *55*, 243–249. [[CrossRef](#)]
22. Cornelius, R.; Heberling, D. Spherical near-field scanning with pointwise probe correction. *IEEE Trans. Antennas Propag.* **2017**, *65*, 995–996. [[CrossRef](#)]
23. Cornelius, R.; Heberling, D. Spherical wave expansion with arbitrary origin for near-field antenna measurements. *IEEE Trans. Antennas Propag.* **2017**, *65*, 4385–4388. [[CrossRef](#)]
24. Saccardi, F.; Rossi, F.; Mioc, F.; Foged, L.J.; Iversen, P.O. Application of the translated-SWE algorithm for the characterization of antennas installed on cars using a minimum number of samples. In Proceedings of the Antenna Measurement Techniques Association Symposium, Atlanta, GA, USA, 15–20 October 2017; pp. 1–6.
25. Mauermayer, R.A.M.; Eibert, T.F. Spherical field transformation above perfectly electrically conducting ground planes. *IEEE Trans. Antennas Propag.* **2018**, *66*, 1465–1478. [[CrossRef](#)]
26. D’Agostino, F.; Ferrara, F.; Gennarelli, C.; Guerriero, R.; Migliozi, M. A Spherical near-to-far-field transformation using a non-redundant voltage representation optimized for non-centered mounted quasi-planar antennas. *Electronics* **2020**, *9*, 944.

27. Bucci, O.M.; Gennarelli, C.; Savarese, C. Representation of electromagnetic fields over arbitrary surfaces by a finite and nonredundant number of samples. *IEEE Trans. Antennas Propag.* **1998**, *46*, 351–359. [[CrossRef](#)]
28. Bucci, O.M.; Gennarelli, C. Application of nonredundant sampling representations of electromagnetic fields to NF-FF transformation techniques. *Int. J. Antennas Propag.* **2012**, *2012*, 319856. [[CrossRef](#)]
29. The CubeSat Program. Available online: <http://www.cubesat.org> (accessed on 2 February 2022).
30. Bucci, O.M.; D'Elia, G.; Migliore, M.D. Advanced field interpolation from plane-polar samples: Experimental verification. *IEEE Trans. Antennas Propag.* **1998**, *46*, 204–210. [[CrossRef](#)]
31. Yaghjian, A.D. Approximate formulas for the far field and gain of open-ended rectangular waveguide. *IEEE Trans. Antennas Propag.* **1984**, *32*, 378–384. [[CrossRef](#)]